This article has been accepted for inclusion in a future issue of this journal. Content is final as presented, with the exception of pagination.

Robust Synthetic Aperture Imaging of Marine Controlled-Source Electromagnetic Data

Xiaolei Tu and Michael S. Zhdanov

***Abstract*—The synthetic aperture (SA) method has recently found applications in the analysis of the low-frequency marine controlled-source electromagnetic (MCSEM) data. It has been shown that this method can enhance the response from an anomalous target. However, in a SA method, anomalous EM fields and the noise will be equally steered and focused, leading to amplifying the noise and introducing artifacts into the images. In addition, the current realizations of the SA method are very sensitive to the noise in the data and the parameters of the SA. In this article, we address these difficulties by introducing a robust SA (RSA) method. The RSA method consists of three steps, namely, robust smoothing of the background field, robust interpolation of EM fields from the real receiver positions to the virtual receiver positions, and estimating the SA weights with a robust optimization scheme. The synthetic model studies show that this method is stable to noise and has a relatively high spatial resolution. We have also applied this method to the towed streamer data collected in the Barents Sea. The generated pseudo-3-D images accurately reveal the locations of the salt domes and fault structures known from the seismic data.**

***Index Terms*—Marine controlled-source electromagnetic (MCSEM), robust norm, synthetic aperture (SA), towedstreamer.**

I. Introduction

SENSITIVE to resistive gas-or-oil-saturated reservoir rocks, marine controlled-source electromagnetic (MCSEM) methods have been widely used in hydrocarbon (HC) exploration and production for derisking and monitoring of the HC deposits [1]–[10]. The recent development of MCSEM survey systems, especially towed streamer acquisition systems, enables the rapid survey of vast areas to locate the potential HC targets [11]–[14]. The development of effective interpretation technique of such massive multitransmitter and multireceiver EM data sets is, therefore, critical for the success of the practical application of the marine EM methods. Numerous research articles have been published on the topic of rigorous inversion of marine EM data to build a 3-D model of subsurface conductivity [15]–[20]. However, large-scale 3-D inversion is still a very challenging problem, and it usually takes several days or even weeks to run the full 3-D inversion on supercomputers. A fast imaging tool is, therefore, preferable, especially for real-time data processing.

Manuscript received August 7, 2019; revised December 1, 2019; accepted January 8, 2020. This work was supported in part by The University of Utah Consortium for Electromagnetic Modeling and Inversion, in part by TechnoImaging, LLC, and in part by the Russian Science Foundation (RSF) under Project 16-11-10188. *(Corresponding author: Xiaolei Tu.)*

Xiaolei Tu is with The University of Utah, Salt Lake City, UT 84112 USA (e-mail: tuxl2009@hotmail.com).

Michael S. Zhdanov is with The University of Utah, Salt Lake City, UT 84112 USA, also with TechnoImaging, LLC, Salt Lake City, UT 84107 USA, and also with the Moscow Institute of Physics and Technology (MFTI), 140342 Zhukovsky, Russia (e-mail: michael.s.zhdanov@gmail.com).

Color versions of one or more of the figures in this article are available online at http://ieeexplore.ieee.org.

Digital Object Identifier 10.1109/TGRS.2020.2966727

Zhdanov *et al.* [21] introduced a rapid imaging method based on the concept of optimal synthetic aperture (OSA), where the map of amplitudes of SA data provides an image of the horizontal distribution of the subsurface geoelectrical structure. The SA is a wave-based concept widely used in radar and sonar imaging. It has been extended to the case of low-frequency diffusive EM field in marine geophysical exploration over the last several years [22], [23]. In the framework of the SA method, the interference effect of EM fields generated by different sources is employed to construct a virtual source with a specific radiation pattern, which would create a constructive interference and increase the signal collected in the area of interest. Fan *et al.* [24] used this technique to steer and focus the EM fields to increase the detectability of the HC reservoir. To determine the optimal parameters of the SA method for marine EM surveys, Yoon and Zhdanov [25] developed an OSA method. They showed that the OSA method would not only improve the resolution of the EM data to the potential targets but also reduce the airwave effect associated with the shallow water EM data. Zhdanov *et al.* [21] adopted the OSA approach to fast imaging the towed streamer EM data by introducing the virtual receivers.

One practical difficulty of the OSA method, however, is that it is sensitive to the background geoelectrical model, which may include varying bathymetry and small local anomalies in the sea-bottom conductivity distribution [26]. A distorted geoelectrical background model unavoidably introduces the artifacts into the OSA image, which may mislead the subsequent data interpretation. In addition, in the OSA method, a constructive interference effect tends to occur where the recorded EM fields are different from what is generated by the background model. The anomalous EM fields and the noise could be equally steered and focused. The area with high noise level but without a subsurface target might be highlighted due to the constructive interference of the noise, leading to a false geological model. The MCSEM surveys, however, are always contaminated by the noise caused by positioning errors, cable tugging, and current flow [27], [28], thus increasing the uncertainty of interpretation.

We propose a robust SA (RSA) method, which is less affected by the choice of the background model and the noise. This new method consists of three steps: 1) robust estimation of the background or reference field; 2) interpolation of the observed data from the real local receivers to the global virtual receivers in a robust way; and 3) calculation of the OSA weights for every source using a robust optimization algorithm. Robust norms are used in all three steps to further suppress the noise. The mathematical representation of the robust norms is provided in the Appendix. For completeness, in Section II, we will review the SA method in common receiver gather and extend it to the common middle point (CMP) gather. The three steps of the RSA method will also be discussed in detail in Section II. We illustrate the effectiveness of the developed method carefully with the synthetic models. We also present a case study for towed streamer EM data collected in the Barents Sea.

II. SA Method

The fundamental concept of the SA method is based on simultaneously processing all geophysical EM survey data via a carefully designed combination of the fields produced by all sources. The superposition of those sources creates a particular interference pattern highlighting the area of interest. We first review the application of the SA method to the common receiver gather considering the case of a typical sea-bottom MCSEM survey.

A. SA Method for Common Receiver Gather

A typical MCSEM survey consists of a set of sea-bottom receivers of the EM field and a horizontal electrical bipole transmitter towed behind a ship. The receivers are fixed at seafloor with the coordinates $\mathbf{x}_l$ ($l = 1, 2, \ldots, L$), where L is the number of receivers. The transmitter, $\boldsymbol{S}_j$, injects a low-frequency current from different locations $\mathbf{x}_j$ ($j = 1, 2, \ldots, J$), where J is the number of source positions. We denote the EM field recorded by the lth receiver corresponding to the jth source injection by d_j^l. The data set $\{d_1^l, d_2^l, \ldots, d_j^l, \ldots, d_J^l\}$ representing the data recorded by the same receiver is, therefore, called a common receiver gather.

The constructed SA source, $\boldsymbol{S}_{\text{SA}}$, is expressed as follows:

$$\boldsymbol{S}_{\text{SA}} = \sum_{j=1}^{J} \tilde{\omega}_j \boldsymbol{S}_j \tag{1}$$

where $\tilde{\omega}_j$ are some optimal source-dependent weights, which steer the EM fields into a designed pattern to illuminate a potential subsurface target the best. The weights, $\tilde{\omega}_j$, are complex numbers, which means that not only the amplitudes of the sources are scaled but also their phases are shifted and aligned to interfere constructively in the area of interest. According to the superposition principle, the SA data, d_{SA}^l, can be expressed as follows:

$$d_{\text{SA}}^l = \sum_{j=1}^{J} \tilde{\omega}_j d_j^l. \tag{2}$$

For simplicity, we rewrite the last equation using the matrix notations as follows:

$$\mathbf{d}_{\text{SA}} = \mathbf{d}\mathbf{w} \tag{3}$$

where $\mathbf{d}_{\text{SA}} = [d_{\text{SA}}^1, d_{\text{SA}}^2, \ldots, d_{\text{SA}}^L]^T$ are the SA data; $\mathbf{w} = [\tilde{\omega}_1, \tilde{\omega}_2, \ldots, \tilde{\omega}_J]^T$ are the weights to be determined; and $\mathbf{d}$ is a matrix of the observed data

$$\mathbf{d} = \begin{bmatrix} d_1^1 & d_2^1 & \cdots & d_J^1 \\ d_1^2 & d_2^2 & \cdots & d_J^2 \\ \vdots & \vdots & \ddots & \vdots \\ d_1^L & d_2^L & \cdots & d_J^L \end{bmatrix}. \tag{4}$$

In the framework of the OSA method, the weights, $\mathbf{w}$, are optimized in order to keep the normalized SA data close to the designed SA (DSA) gate if a subsurface anomaly is present, and equal them to unit 1 in the absence of the subsurface target [21], [25].

The SA concept can also be applied to the receivers by creating the SA receiver. We construct the SA receiver in the common source gather. In this case, the SA represents spatially distributed receivers, which simultaneously record the EM field generated by a transmitter from a single location. Note that, Tu [29] employed a similar approach to reduce the noise and improve the EM data quality in the time domain by using the weights calculated in logarithmic space based on Maxwell's equation.

B. SA Method for CMP Gather

A CMP is a point on the surface halfway between transmitter and receiver. In an MCSEM survey with regular offsets and source intervals, there may be several transmitter–receiver pairs sharing the same CMP. A CMP gather is a data set associated with such transmitter–receiver pairs. Fig. 1 shows four transmitter–receiver pairs of a towed streamer EM survey, which generates a CMP gather of four data points. We can compose an SA receiver from all four receivers and an SA source from the four sources.

A general expression of SA data, d_{SA}, incorporating both SA source and receiver is presented as follows:

$$d_{\text{SA}} = \sum_{j=1}^{J} \tilde{\omega}_j \left(\sum_{l=1}^{L} w_j^l d_j^l \right) \tag{5}$$

where J denotes the number of sources; $\tilde{\omega}_j$ are the same as in (1); L represents the number of receivers; w_j^l are the receiver-dependent weights. The superposition, $\sum_{l=1}^{L} w_j^l d_j^l$, combines an array of the receivers into one SA receiver. Note that the SA receiver is created for the common source gather. The SA weights, w_j^l, can be source-dependent to accommodate the survey configurations and to create a desired interference pattern.

Setting $w_j^l = \delta(i, j)$ (the Kronecker delta function), we would arrive at an SA expression for CMP gather

$$d_{\text{SA}} = \sum_{j=1}^{J} \tilde{\omega}_j d_j^j \tag{6}$$

This article has been accepted for inclusion in a future issue of this journal. Content is final as presented, with the exception of pagination.

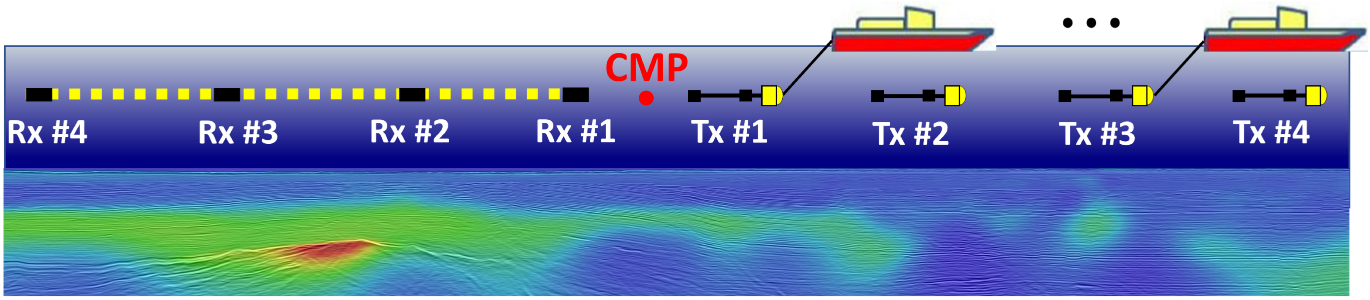

Fig. 1. One CMP shared by four transmitter–receiver pairs in a towed steamer EM survey. The red point denotes the position of the CMP. Rx is the abbreviation of receivers (denoted by big black squares) mounted in a towed steamer cable. We indicate the cable with a yellow dashed line to show that the receiver could be both real and virtual. Transmitter, abbreviated to Tx, is towed by a ship, together with the cable. The CMP is the geometric middle point of pairs (Tx#1, Rx#1), (Tx#2, Rx#2), (Tx#3, Rx#3), and (Tx#4, Rx#4).

where d_j^j is the data recorded by the jth receiver, while the EM field is generated by the jth source so that all Jth data points are associated with the same CMP.

Equation (6) can be rewritten in the same form as (2) or more compactly as (3) with d_j^l representing the data associated with the lth CMP and jth transmitter position. The SA method in the CMP domain, however, is physically different from that for the common receiver gather. The former involves the concept of constructing SA receivers from a known receiver array, besides the designing OSA sources.

One should note that a similar technique of data processing has been widely used in seismic methods to perform CMP stacking to increase the signal-to-noise (SN) ratio. However, (6) presents a more general approach by computing the optimal amplitude scale and phase shift parameters according to a predesigned interference pattern of the field.

The RSA method consists of three steps. We describe these steps for CMP gather based on the case of a towed streamer EM survey.

C. Robust Background Field Smoothing

The EM field decays rapidly in seawater with the increase of the transmitter–receiver distance (i.e., offset), making it challenging to identify an anomaly associated with the HC reservoir. The observed and SA data have to be normalized by a background field to improve the detectability of a reservoir.

There are two different ways to determine the background EM field [21]. One is based on a background geoelectrical model, which is usually set as a horizontally layered medium. The background model can be built using the 1-D inversion of the observed data. Another way is to use the EM field observed far enough from the area of interest as the reference field. This method does not need any prebuilt model or 1-D inversion. Such a reference field, however, is always contaminated with the noise and effects of local geoelectrical inhomogeneities in the location of the reference observation point. This noise and the effects of the local anomalies can then be steered and amplified by subsequent SA steps, leading to artifacts in the SA images. Denoising should be applied to the reference field before further processing.

We apply the robust smoothing to the background field before performing the normalization. The robust smoothing can be formalized as the minimization of the following parametric functional:

$$\mathrm{p}^{\alpha}(\mathbf{d^b}, \widetilde{\mathbf{d^b}}) = \|\widetilde{\mathbf{d^b}} - \mathbf{d^b}\|^2 + \alpha\|\mathbf{R}\widetilde{\mathbf{d^b}}\|^2 \rightarrow \min \tag{7}$$

where $\mathbf{d^b}$ and $\tilde{\mathbf{d^b}}$ are the vectors of original and smoothed background fields, respectively; $\mathbf{R}$ is the roughness operator, which is the second-order differential operator; and α is a regularization parameter. This optimization problem is solved using the reweighted regularized conjugate gradient (RRCG) method developed in [30]. The robust smoothing acts in a way similar to the spatial low pass filter [31]. The environmental noise and responses from the local geoelectrical inhomogeneities are removed as well.

D. Robust Interpolation of EM Fields

In a real marine survey, the configuration is seldom regular, especially for a towed streamer EM survey. The receiver positions vary from one transmitter position to another, and their intervals are irregular due to cable feathering. The CMPs, therefore, change with the transmitter positions. A shared CMP is required for a set of transmitter–receiver pairs to apply the SA method for a CMP gather. The fundamental concept of the SA method is that the signals generated by the sources at different positions are measured at the same receiver positions, so that they can be integrated to increase the potential anomaly [21]. Unlike the conventional MCSEM system, the towed streamer system consists of a set of towed receivers, which can measure a signal generated at a certain transmitter position only. In order to integrate the signals generated by different sources at the same receiver positions in the towed streamer EM system, we have to interpolate and/or extrapolate the fields from each source to the virtual receiver positions, which can be shared by all the transmitter shots. Note that the concept of a virtual receiver is also quite common in radar applications [21].

Even if we have applied denoising to the background field, the normalized field is nevertheless not noise-free. The noise from the total field and the remnants of background field denoising together add up to the noise level of the normalized field. The conventional interpolation operators are local operators, and they are usually very sensitive to the noise in the data. A small amount of noise or a few outliers in the data will distort the interpolated fields in the virtual receivers. This is especially the case for the data with a strong spatial variation, which usually corresponds to the lateral contrast in the sea-bottom geoelectrical properties in our case. The variations in the interpolated field would be blurred and have fuzzy boundaries. Thus, the spatial resolution of the SA method would be damaged. Furthermore, the distortions could also be amplified by the SA weights, propagate to the SA data, and result in fictitious EM anomalies.

Alternatively, a global interpolation operator, which we call robust smoothing interpolation, introduced to make the field interpolation from the actual receiver positions to the virtual receivers is more robust. The robust smoothing interpolation is defined as the minimization of the following parametric functional:

$$p^{\alpha}(\boldsymbol{d}, \boldsymbol{d}^{v}) = \|\boldsymbol{d}^{v} - \boldsymbol{P}\boldsymbol{d}\|^2 + \alpha\|\boldsymbol{R}\boldsymbol{d}^{\boldsymbol{v}}\|^2 \rightarrow \min \tag{8}$$

where $\mathbf{d}^{\mathrm{v}}$ is the vector of the interpolated fields in the virtual receivers, and $\mathbf{d}$ is the vector of original fields at the actual receivers. $\mathbf{P}$ denotes the conventional interpolation (linear or spline) operator. $\mathbf{R}$ is the roughness operator. The optimization problem is also solved using the RRCG method.

The robust smoothing interpolation is a global operator, which relates the current interpolated value to not only its neighbors but also to all the sampling points involved. Thus, the interpolated field is enforced to follow a general trend in the data without being affected by the local outliers. The smoothing regularization term can also help denoise the interpolated field. In this way, the fields calculated in the virtual receivers are less biased by the noise.

Note that, in (7), (8), and (10), one should select the proper value of the regularization parameter, α. This parameter is adaptively determined by the RRCG method. The basic idea is that it is calculated at the first iteration so that the misfit and regularization terms are equally weighted, and then, α gradually decreases in the following iterations using the geometrical progression until the misfit condition is reached [30].

E. RSA Weights

To steer the EM fields toward the potential targets, we follow the idea of the OSA method [21], [25] by designing the RSA weights that automatically enhance the anomalous field from the potential HC reservoir. As demonstrated in the refereed articles, this can be effectively achieved by minimizing the misfit between the normalized SA data, $\mathbf{d_R}$, and a pre-DSA gate.

The normalized SA data, $\mathbf{d_R}$, are defined as the element-wise ratio between the SA data and the SA background fields

$$\mathbf{d_R} = \left[d_{\mathrm{SA}}^1/d_B^1, d_{\mathrm{SA}}^2/d_B^2, \ldots, d_{\mathrm{SA}}^L/d_B^L\right]^T \tag{9}$$

where L denotes the number of CMPs; $d_B^l = \sum_{j=1}^{J} \tilde{\omega}_j \tilde{d^b}_j^l$ represents the SA background field with $\tilde{d^b}_j^l$ being the interpolated smoothed background field associated with the lth CMP and jth transmitter position; and d_{SA}^l are the SA data in the CMP domain, as defined in (2). Note that, by setting all the SA weights $\tilde{\omega}_j$ to 1, we arrive at the SA data, $\mathbf{d_R}$, without steering. The SA data calculated with RSA weights are called the RSA data.

The RSA weights can be found by solving a minimization problem for the corresponding parametric functional

$$\mathrm{p}^{\alpha}(\mathbf{D}, \mathbf{w}) = \|\mathbf{D} - \mathbf{A}(\mathbf{w})\|^2 + \alpha\|\mathbf{RA}(\mathbf{w})\|^2 \rightarrow \min \tag{10}$$

where $\mathbf{A}(\mathbf{w}) = \mathbf{d_R}$ is the forward operator for the normalized SA data, acting on the RSA weights, $\mathbf{w}$; $\mathbf{D}$ represents the pre-DSA gate, which is designed to enhance the anomalous response from the potential targets. We can set it to a boxcar function with a maximum over the expected area of an HC reservoir. In the case of a reconnaissance survey, it is reasonable to select a uniform DSA with the constant value greater than one to enhance the anomalies, present in the survey area. We also introduce a smoothing regularization term that favors smoothed SA data. We still resort to the RRCG method to solve the minimization problem (10).

One can easily calculate the SA data, $\mathbf{d_R}$, using (9), once the optimal RSA weights are found.

III. Robust Norms

The least-squares norm (L_2-norm) is the most commonly used metric in the solution of the geophysical inverse problem. However, it has long been understood that the fundamental underlying hypothesis (i.e., Gaussian uncertainties) for least-squares criterion is generally not satisfied because of the long-tailed density functions in data and model uncertainties [32]. Alternatively, the L_1-norm is considerably less sensitive to large measurement errors and more appropriate to long-tailed probability density functions. Considering the ill-posed nature of the geophysical inverse problem, it is expected that the less noise-sensitive metric generally yields a far more stable estimation of the model parameters than the least-squares norm [33], [34].

The L_1-norm of the residual vector $\mathbf{r} = (r_1, r_2, \ldots, r_n)^T$ is defined as follows:

$$\|\mathbf{r}\|_{L_1} = \sum_{i=1}^{n} |r_i|. \tag{11}$$

This function is known to be nonsmooth: it is singular where any of the residual components vanish [34], causing difficulties for numerical optimization. These drawbacks of L_1-norm led to a group of robust norms, such as Huber norm, Hampel norm, and Tukey bisquare norm. Their general idea is to combine different treatments of residuals together. Usually, small residuals are considered to be more "important" than big ones. The robust norm is considerably less sensitive to large measurement errors and more appropriate for a long-tailed probability density functions [33]. Their applications in geophysics are extensive. For example, Chave *et al.* [35], Egbert and Booker [36], Jones *et al.* [37], and Sutarno and Vozoff [38] introduced the robust M estimation of magnetotelluric impedance tensor based on the robust norm; Guitton and Symes [34] applied the Huber norm to the velocity analysis of seismic data. The robust norm can be introduced as a weighted least-squares norm.

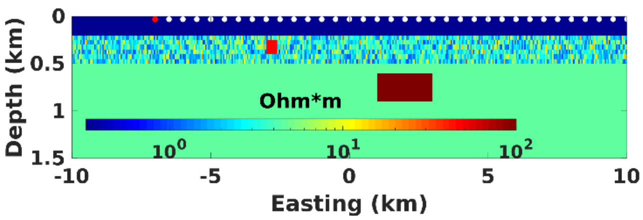

Fig. 2. Vertical section of Model 1. The second layer contains some geological (model) noise and a small anomaly with a resistivity of 50 Ω-m. A reservoir of 100 Ω-m is embedded in the basement layer. The dots denote the transmitter positions. The electric field associated with the transmitter position denoted by the red dots is chosen as the reference field.

In a general case, an arbitrary robust norm of the residual vector $\mathbf{r} = (r_1, r_2, \ldots, r_n)^T$ can be given by the following formula:

$$\|\mathbf{r}\|_\rho^2 = \sum_{i=1}^{n} |\rho_i(\mathbf{r})|^2 \tag{12}$$

where $\rho_i(\mathbf{r})$ are the functions determining the properties of the corresponding robust norm. Expression (12) can also be written as a quasi-quadratic functional as follows:

$$\|\mathbf{r}\|_\rho^2 = (\mathbf{W}_\rho \mathbf{r}, \mathbf{W}_\rho \mathbf{r}) \tag{13}$$

where $(\ldots, \ldots)$ represents the inner product in the corresponding function space, and $\mathbf{W}_\rho$ is a diagonal weighting matrix of the robust norm with the following components:

$$W_{\rho i}(\mathbf{r}) = \frac{\rho_i(\mathbf{r})}{(|r_i|^2 + e)^{\frac{1}{2}}} \tag{14}$$

where $e > 0$ is a small number introduced to avoid the singularity.

The expression of general robust norms and their representations in the forms of quadratic functionals can be found in Appendix.

Note that, the misfit functionals in (7), (8), and (10) were calculated with L_2-norm. We can make them more robust by employing the robust norms introduced above.

IV. Synthetic Model Study

A. Robustness to Noise

In this section, we demonstrate that the proposed method has a strong resistance to the noise both in the data and in the model.

We consider a three-layered shallow water model consisting of 200-m sea-water layer with a resistivity of 0.33 Ω-m, a sediment layer with a thickness of 300 m, and a half-space basement of 3 Ω-m. Fig. 2 presents a vertical section of the model. We assume a random resistivity distribution for the sediment layer to simulate the real-world model noise. This layer also contains a shallow small anomaly of 50 Ω-m. The sizes of the anomaly are 350 m × 500 m × 100 m. A reservoir with sizes of 2 km × 1 km × 3 00 m is located at a depth of 600 m below the sea level. The resistivity of the reservoir is 1000 Ω-m (see Fig. 2). The towed streamer EM survey consists of one survey line, running in the x-direction at $y = 0$. A horizontal electric dipole transmitter oriented in the x-direction with a moment of 1 Am is towed

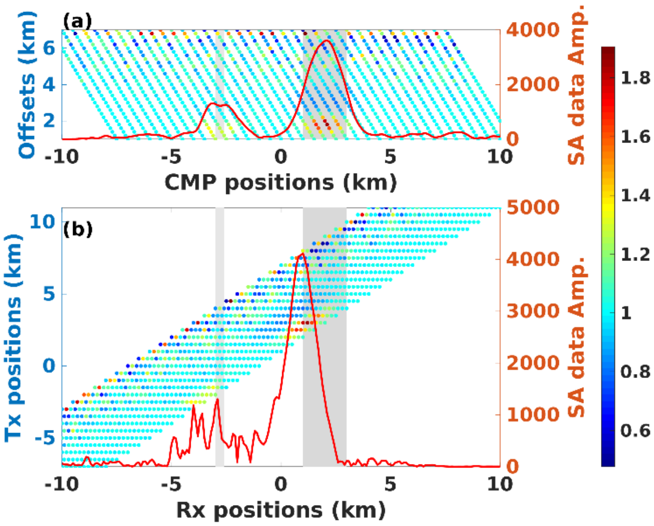

Fig. 3. Amplitude of normalized Ex field in (a) CMP and (b) CRP domains. The gray areas represent the horizontal locations of the two anomalies. The red lines denote the amplitudes of the corresponding SA data in CMP and CRP domains, respectively.

from −7 to 11 km in the x-direction at a depth of 10 m below sea level. The transmitter is set to inject 1-Hz EM signal into the seawater at every 500 m. Thirty-one receivers with offsets between 1 and 7 km are towed at a depth of 100 m and measure the in-line electric fields at a frequency of 1 Hz. We have contaminated the synthetic data with the Gaussian noise with a spectral density of 4×10^{-14} V/[m $\cdot \sqrt{\text{Hz}}$] [27].

Totally 37 transmitter positions along the survey line were employed to construct the SA source. The data observed for the first source located at −7 km (denoted by the red dot in Fig. 2) were selected as the reference fields. We present the amplitudes of the normalized fields in the CMP and the common receiver point (CRP) domain in Fig. 3. Responses in the CMP domain show a better correlation with the true horizontal location of the resistors. We also observed a strong correlation between the SN ratio of the normalized fields and offset. The SN ratio is lower for large offsets. We could, therefore, assign smaller weights to large offsets data to decrease their influence on the SA images. This could be more conveniently implemented with the CMP domain representation than that of the CRP domain. We calculated the OSA weights and the SA data both in CMP and CRP domain for comparison. The amplitudes of SA data are shown with red lines in Fig. 3. The CMP domain responses correlate with the true horizontal location of the anomalies much better and are less affected by the noise. We also present a comparison of the SA results computed with different methods both in CMP (left) and CRP (right) domains in Fig. 4. The red lines in Fig. 4(a) and (b) represent the amplitude of OSA data following [25]. The amplitude of RSA data produced using L_2-norm and Huber norm for the misfit functionals are plotted in Fig. 4(c)–(f), respectively. We also computed the SA data with the RSA method without steps 1 and 2, with their amplitudes shown in Fig. 4(g)–(j), respectively. The DSA gate is presented in the cyan solid line. The response of the big reservoir is enhanced in all methods in both CMP and CRP domains. The shallow small anomaly is only well imaged by the RSA method in the

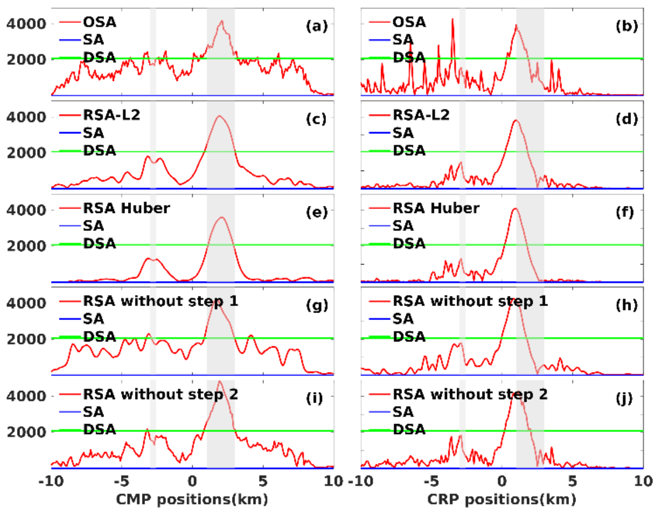

Fig. 4. Amplitudes of the SA data with different methods in (Left) CMP and (Right) CRP domains. The gray areas show the horizontal locations of the two anomalies. The Blue line in all panels represent the result of SA method without steering. The green line denotes the designed SA. The red lines in (a) and (b) are the results of OSA method; in (c) and (d) are results of RSA method with L_2 norm. The results obtained with RSA method with Huber norm are shown by red lines in (e) and (f). The results of RSA method with Huber norm but without steps 1 and 2 are also presented in (g) and (h), (i) and (j), respectively.

CMP domain. The RSA method with the Huber norm produces the best result. We also observed that CRP domain methods are more resistive to noise than those in the CMP domain.

B. Spatial Resolution

In the next synthetic study, we consider a series of models containing two anticline-associated reservoirs with different horizontal distances to demonstrate the spatial resolution of the RSA method. We should note that in a general case, the RSA method could smooth out small local anomalies because we employ a robust interpolation in the second step, which works like a low pass filter. However, the parameters of the RSA method could be adjusted by choosing a proper robust norm in order to resolve the closely located targets.

The background of the models consists of four layers: a 200-m seawater layer with a resistivity of 0.33 Ω-m, the second layer of a 300-m thickness with a random distribution of resistivity, a basement of 10 Ω-m, and a relatively conductive 3-Ω-m layer embedded in the basement with a depth from 1200 to 1400 m. Two anticline-associated reservoirs of the same sizes, about 2 km × 1 km × 0.3 km, are buried at a depth from 700 to 1000 m. They are aligned with each other in the y-direction centered at $y = 0$. We also set a shallow small resistive lens structure at a depth of about 600 m. In our model study, we gradually decrease the distance between the two reservoirs from 3 to 0 km. The observed data were all contaminated with the Gaussian noise with a noise level of 4×10^{-14} V/[m $\cdot \sqrt{\text{Hz}}$] and processed using different versions of the SA method.

We use the same survey design as for Model 1. Fig. 5 shows the SA results for four different spatial distances, 3, 2, 1, and 0 km, respectively. The blue solid lines denote the RSA results with the robust Huber norm. The red solid lines present the RSA results with L_2-norm. The cyan solid lines represent the conventional OSA results. The green solid lines show the SA data without steering. The results demonstrate that the RSA method generally has better spatial resolution than the OSA method. At the same time, for the RSA method with different norms, the robust norms work better than the L_2-norm. A comparison of SA responses with different methods in both the CMP and CRP domains is also presented in Fig. 6. The RSA results without either step 1 or step 2 again show decreased resolution and SN ratio.

C. Salt Dome Model

We now report the results for SA imaging of a realistic model. The marine model contains two deeply buried salt domes and a shallow turtleback oil reservoir in between. Fig. 7 presents a 3-D view of the model. There is a conductive layer embedded in the resistive basement. The layer is mostly flat but folded to a shallower depth around the salts and in the central minibasin. The second layer is also of random resistivity distribution, as shown in the vertical section in Fig. 8(b).

As illustrated in Fig. 8(a), a 3-D survey consisting of 33 survey lines with a spacing of 500 m is designed to image the geology. The transmitter is oriented in the x-direction and towed from $x = -9$ km to $x = 15$ km with a source interval of 400 m. The EM signal of six frequencies from 0.1 to 10 Hz is transmitted and received. The in-line electric field was synthesized with the integral equation method and contaminated with the Gaussian noise as in previous models. We chose the data associated with the most southeast source as the reference field [indicated by the black dot in Fig. 8(a)]. We selected a constant DSA of 1000 for a blind test (i.e., excluding any *a priori* information about subsurface geology). We then applied different SA methods (SA without steering, OSA, and RSA with different norms) to the synthetic data. As a result, we obtained the SA data for all the survey lines and frequencies. The map of amplitudes of SA data for each frequency component constitutes an SA image, providing horizontal distributions of geoelectrical structures at depth.

EM field of different frequencies penetrates the Earth into a different depth and is sensitive to geoelectrical anomaly within different depths. SA images of different frequencies can, therefore, provide the depth information and have a vertical solution. We transform frequency to pseudo depth based on the integrated sensitivity of the common source gather to subsurface conductivity. Following [30], the integrated sensitivity of the data to the conductivity of depth z_k can be calculated as follows:

$$S_k = \frac{\|\delta \mathbf{d}\|}{\delta \sigma_k} = \sqrt{\sum_i |F_{ik}^b|^2} \quad (15)$$

where $\delta \mathbf{d}$ is the variation of a common source gather; $\delta \sigma_k$ denotes the perturbation of conductivity at depth z_k; and F_{ik}^b represents the sensitivity of data point at the ith offset to conductivity at depth z_k calculated from the 1-D background model. The pseudo depth for each frequency is defined as the depth, where the integrated sensitivity decreases to 1% of its maximum value, as illustrated in Fig. 9. The defined pseudo

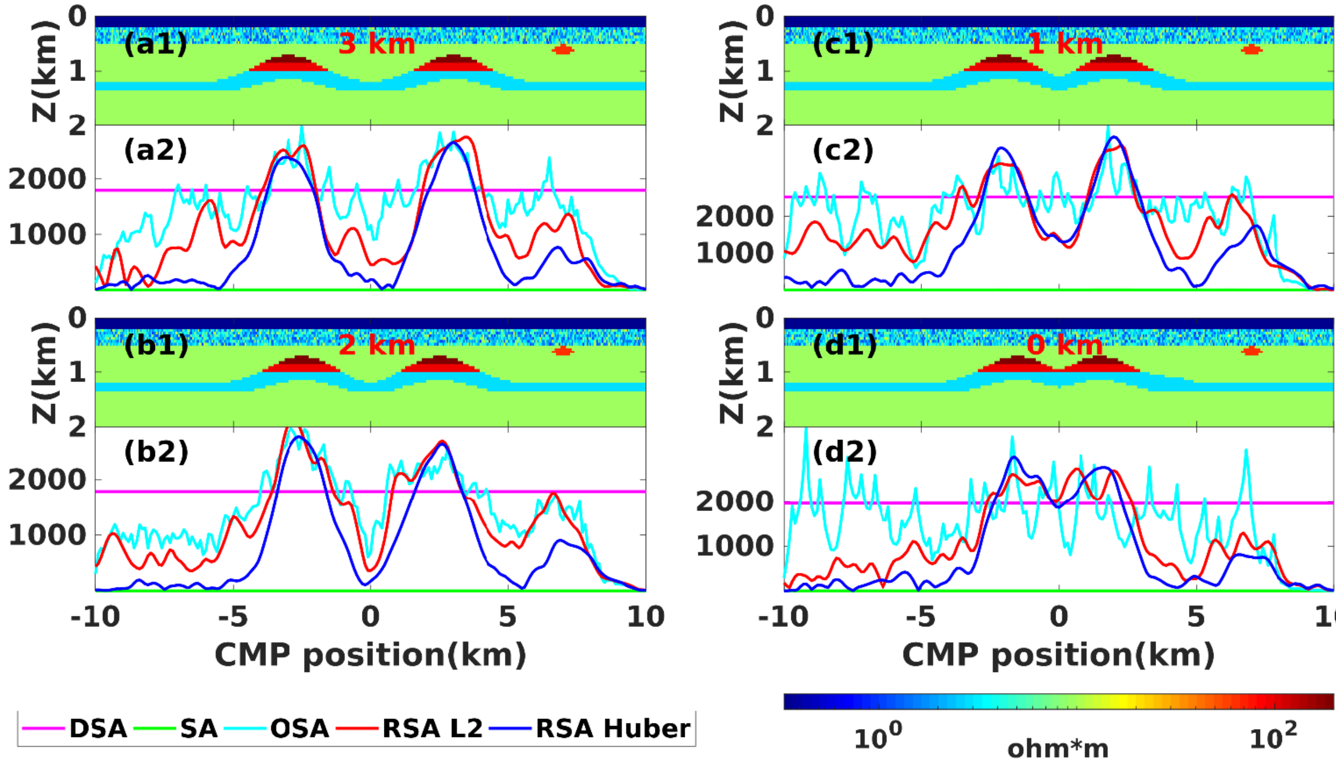

Fig. 5. Anticline models and the corresponding SA data amplitudes. The horizontal distances between the two anticlines are 3, 2, 1, and 0 km for (a1), (b1), (c1), and (d1), respectively. There is also a lens structure at a shallower depth. The second layer is also contaminated with geological noise. The SA response without steering (denoted by the green solid line) is too weak to be seen in the figure.

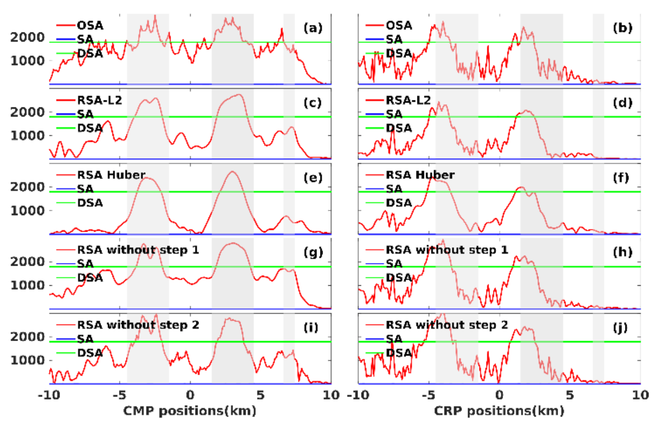

Fig. 6. Amplitudes of the SA data with different methods in CMP (left) and CRP (right) domains for anticline model in Fig. 5(a1). The gray areas show the horizontal locations of the anomalous targets.

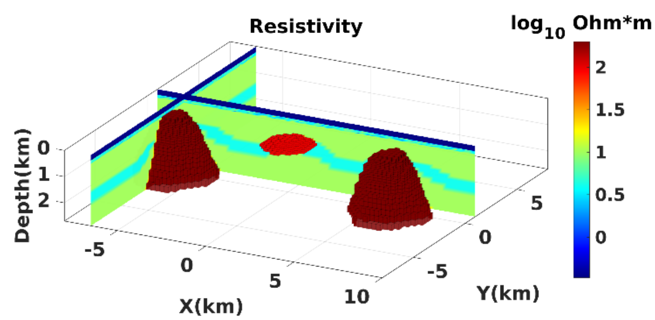

Fig. 7. 3-D view of the salt dome model. The two salt domes are symmetric with each other, with a resistivity of 200 Ω-m. The conductive layer with a resistivity of 4 Ω-m is almost flat but fold up around the salt domes and in the center of the survey area. A turtleback oil reservoir with a resistivity of 100 Ω-m is located in the center of the minibasin between the two salt domes. The thickness of the second layer is about 130 m. It also contains some geological noises as in previous studies.

depth is similar to skin depth, except that the former is based on the sensitivity of a 1-D background model and a specific survey configuration.

We present the SA images in pseudo-3-D maps, with the frequency being the z-axis in frequency-decreasing order from top to bottom. As lower frequencies are transformed into deeper depths, such maps may well provide depth information about the subsurface geoelectric structures. Fig. 10 presents the SA images obtained by the SA method without steering. Figs. 11–13 show the SA images produced by the OSA method, the RSA method with L_2-norm, and the RSA method with L_2-norm, and with the RSA method with Huber norm, respectively. Maps of the true resistivity model at the corresponding pseudo depths are also shown in Fig. 14 for comparison. Although the horizontal locations of the salt domes are reasonably recovered in Fig. 10, their boundaries are blurred. Due to the weak amplitudes of the response from the salt domes and the reservoir, the images are fuzzy, especially for high-frequency components. The amplitude of the response from the anomalies can be strongly enhanced by the OSA method, as shown in Fig. 11. Note the different colorbar scales used in Figs. 10 and 11. The geometry of the salt domes is though not well-confined. Figs. 12 and 13 depict the SA images by the RSA method with L_2-norm and Huber norm, respectively. Both recover the shape of the salt domes very well and less affected by

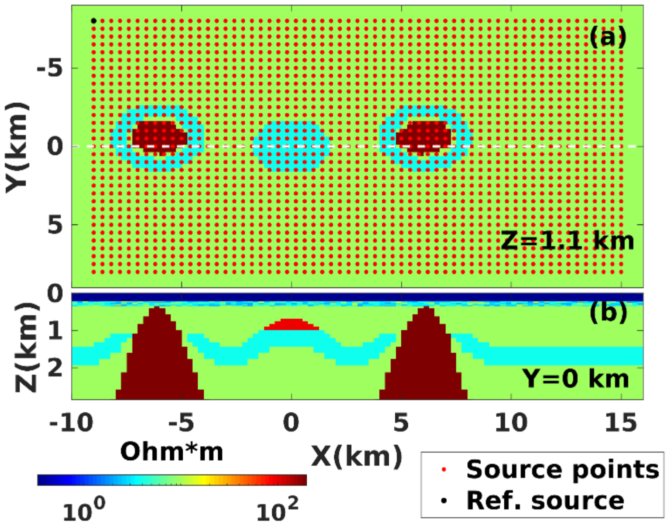

Fig. 8. (a) Horizontal and (b) vertical slices of the salt dome model. The turtle back oil reservoir is located in the center of the minibasin. The transmitter positions are also shown in (a); common source gather associated with the black dot is chosen as the reference field.

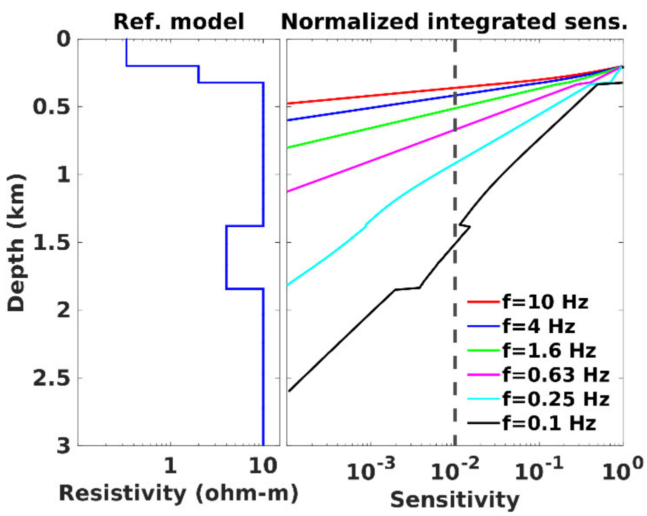

Fig. 9. 1-D reference model for the salt dome model and the integrated sensitivity for each frequency component. Two panels share the same abscissa of depth.

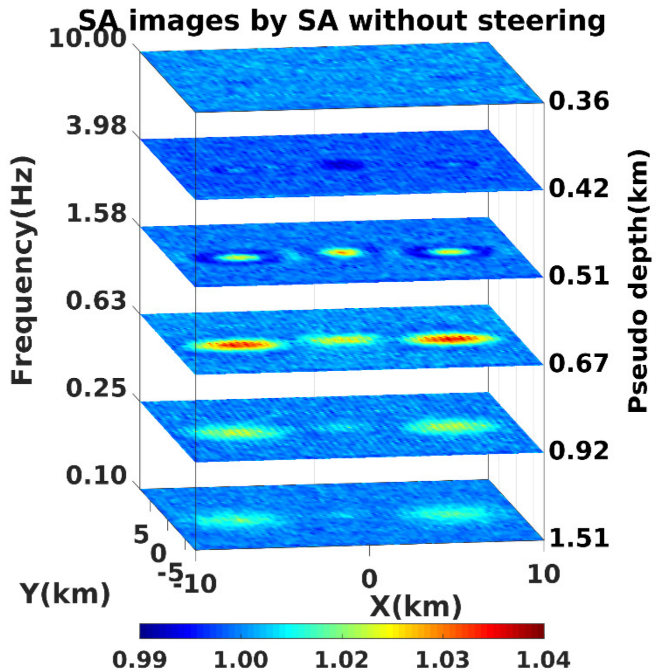

Fig. 10. SA images by the SA method without steering, where the decreasing frequencies are transformed to increasing pseudo depths. Images of higher frequencies corresponding to shallower depths are displayed on the top of the 3-D image volume, whereas those of lower frequencies are displayed on the bottom.

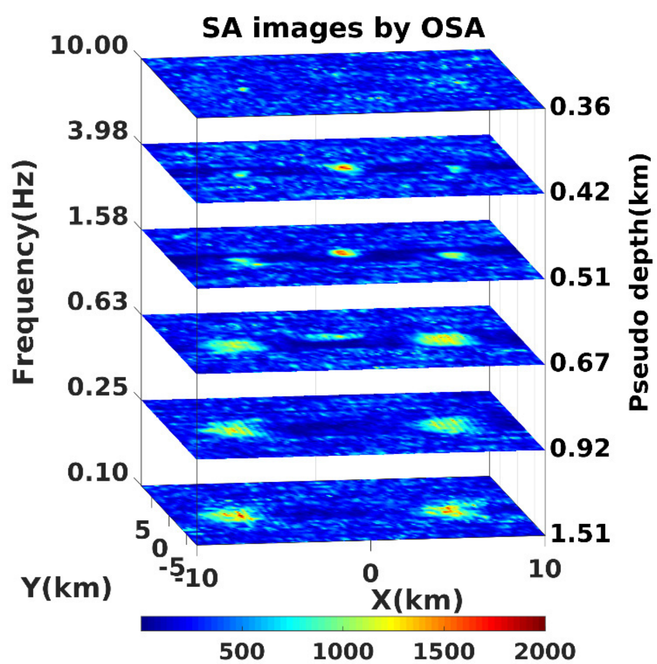

Fig. 11. SA images by the OSA method.

the noise. The latter produces a slightly higher contrast of the reservoir and salt domes with background, is therefore more robust to noise in the data.

As OSA method [21], the RSA method is computationally efficient. It took only a few seconds using a PC with Intel Core i7 CPU at 2.4 GHz and 8-GB memory to compute the RSA data for the dense survey in this case, while a rigorous 3-D inversion of the same data set required several hours or even days of computation on a cluster.

V. Case Study

We have applied the OSA method to the towed streamer EM data collected by PGS in the Barents Sea. There is a known salt dome structure located at almost the center of the survey area; however, its shape is unclear. We have investigated how the OSA method might help to enhance the EM response from this salt dome, which is more resistive than the surrounding sea-bottom sediment.

Fig. 15 presents a bathymetric map of the survey area. The sea bottom is gradually west-dipping, with an uplift in the central part and a subbasin to the west of the uplift.

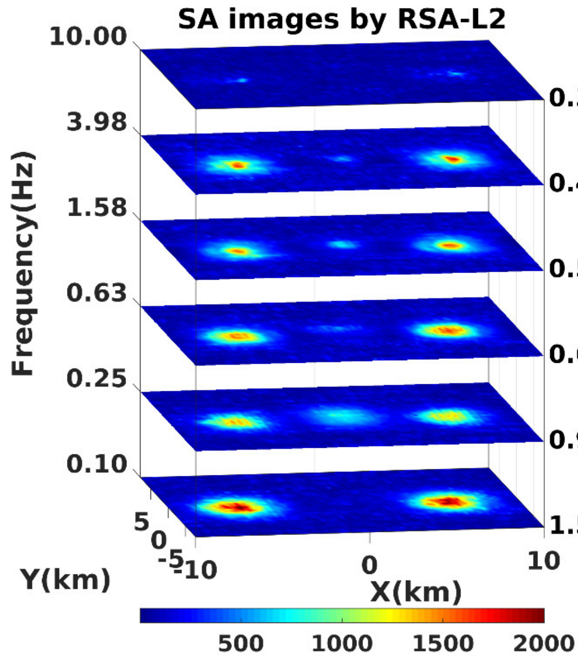

Fig. 12. SA images by the RSA method with L_2-norm.

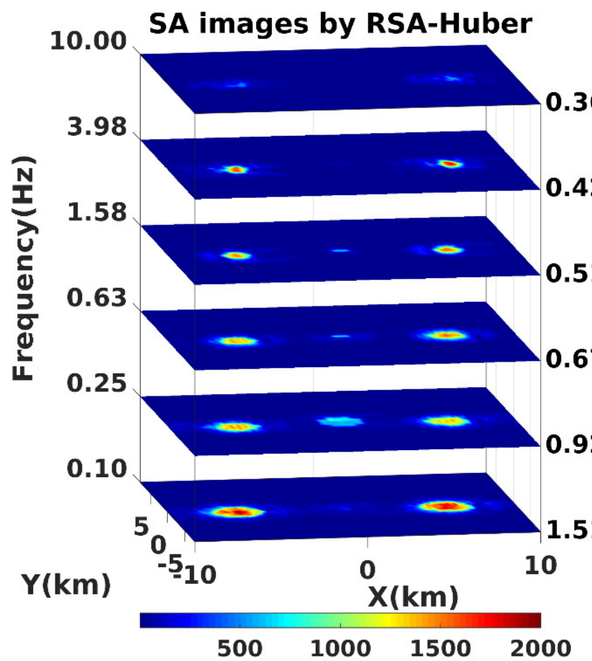

Fig. 13. SA images by the RSA method with the Huber norm.

Two northward trenches enclose the central uplift to the west and east.

The towed streamer EM data used in this study were collected at seven survey lines at six frequencies of 0.2, 0.4, 0.8, 1.4, 1.8, and 2.6 Hz. The 8700-m-long EM streamer was towed at a depth of approximately 100 m below the sea surface. Twenty-three receivers with offsets between 2057 and 7752 m were selected. The electric current source was towed at a depth of approximately 10 m below the sea surface. Fig. 16 presents the profiles of the amplitude of the observed

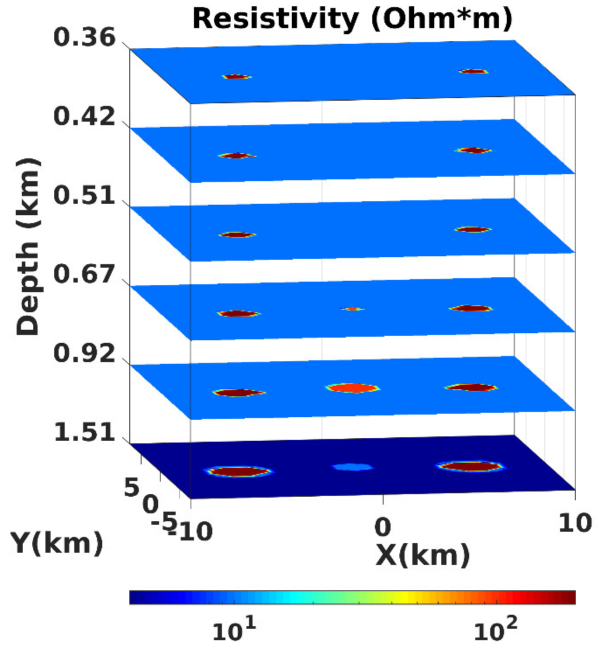

Fig. 14. Horizontal slices of true model at the corresponding pseudo depths for six frequency components.

inline electric field for frequency components 0.2 and 1.4 Hz with a common offset of 5.4 km.

We selected the source gather associated with a source at the southmost survey line as the reference field (red dot in Fig. 11). The reference source was located at the center of the flat subbasin, far from any variation of the seafloor terrain. The generated reference field is, therefore, supposed to be least affected by the sea-bottom anomalies. To preclude the influence of the bathymetry on the SA images and to enhance the response from the salt dome in the central part of the survey area, we chose a DSA as a boxcar function, which is equal to 1 over the entire domain except for an interval from $X = 20$ km to $X = 60$ km, where it is equal to 1000.

We have applied the OSA and RSA methods with L_2-norm and robust norms to the survey data for each frequency. As a result, we have received an SA image for each method and each frequency. We have also transformed the frequencies to pseudo depth via the 1% of maximum integrated sensitivity criteria as in the previous model study.

The integrated sensitivity was calculated using a 1-D background geoelectrical model derived from the 1-D inversion of the reference EM field. As shown in Fig. 17, the decreasing frequency is associated with enhanced sensitivity at depth, particularly below 1.5 km, enabling a sensitivity-based transform of frequency to pseudo depth.

We present the SA images in a frequency decreasing order from the top to the bottom, as in the previous model study. The images produced by the SA method without steering reveal an anomaly in the central part of the survey area (see Fig. 18); however, the magnitude of the anomalous response is tiny, and its shape changes inconsistently with the frequency. In addition, the images are dominated by the

This article has been accepted for inclusion in a future issue of this journal. Content is final as presented, with the exception of pagination.

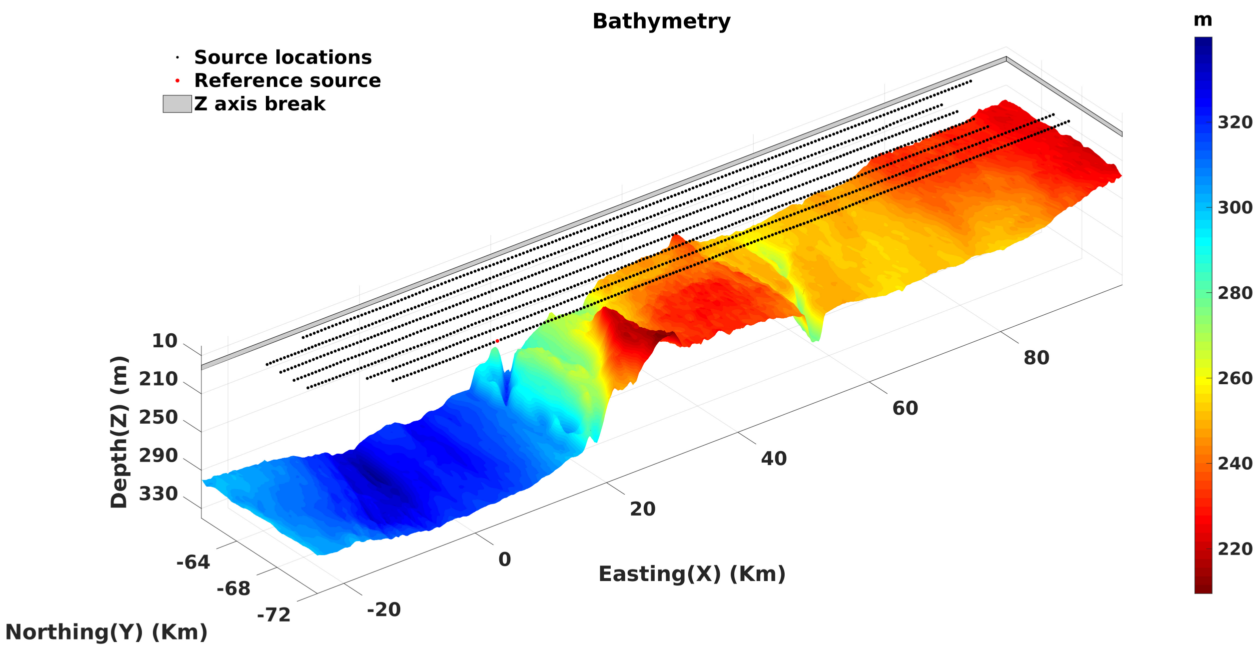

Fig. 15. Bathymetry of the survey area and the transmitter locations. Common source gather associated with the red dot is chosen as the reference field.

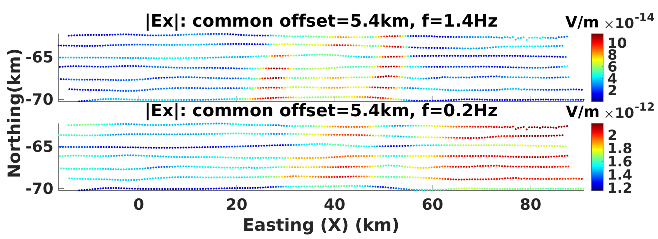

Fig. 16. Amplitude of the observed data of frequency components 1.4 and 0.2 Hz with a common offset of 5.4 km.

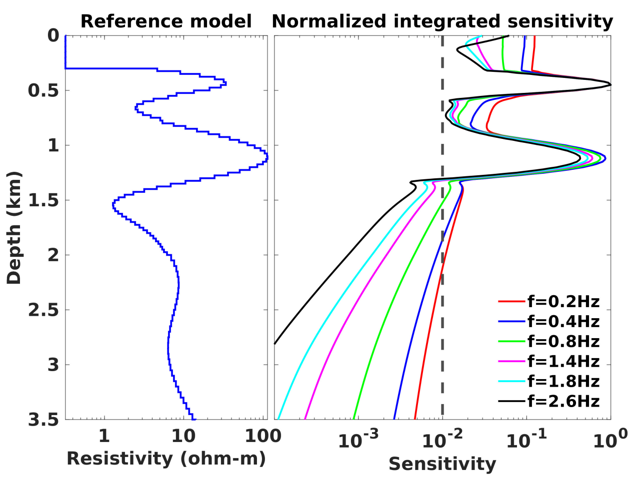

Fig. 17. Inverted 1-D model and the integrated sensitivity for each frequency component based on it. Two panels share the same abscissa of depth.

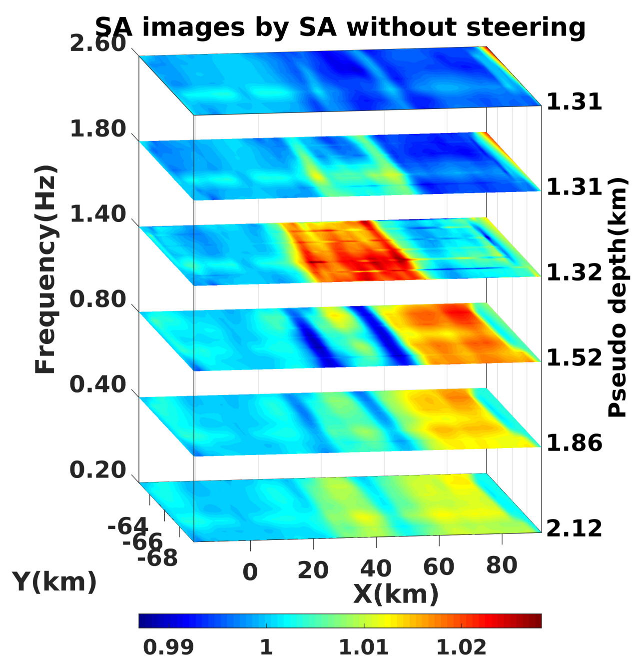

Fig. 18. SA images by the SA method without steering with a frequency decreasing order from top to bottom. The frequencies as shown in the z tick values on the left side are transformed to pseudo depths on the right side.

response from the bathymetry and the noise in the data. The OSA method enhances the response from the salt dome in the central area and suppresses the influence of the bathymetry, as demonstrated in Fig. 19. It also brings out two linear structures (indicated by black dashed lines in Fig. 19), which we interpreted to be two faults controlling the boundaries of the salt dome. Their locations coincide well with those of the two trenches on the bathymetric map. These geological features are more prominent in the images produced by the RSA method with Huber norm, as shown in Fig. 20. These observations demonstrate well the ability of the OSA and RSA methods to enhance the response from the target, while the RSA images provide a slightly better horizontal resolution compared to the OSA method.

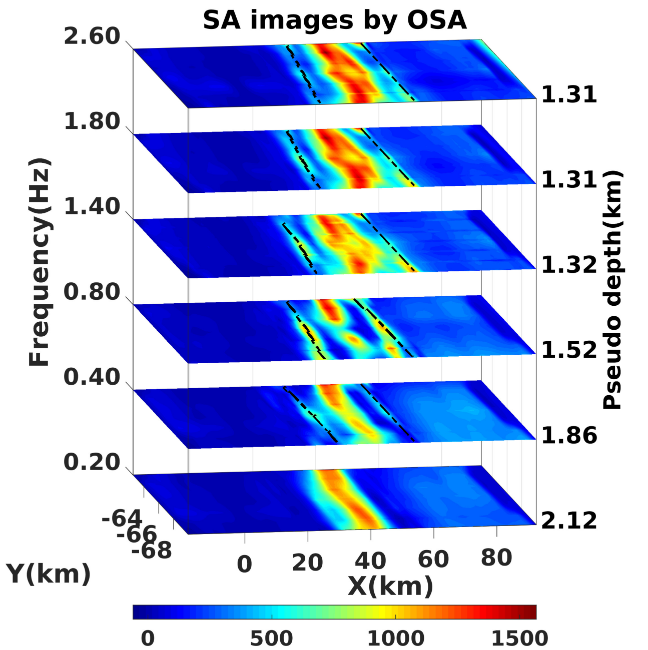

Fig. 19. SA images by the OSA method with a boxcar DSA uplifting the response from the salt dome in the central part. The black lines denote the interpreted locations of the two faults controlling the boundary of the salt dome.

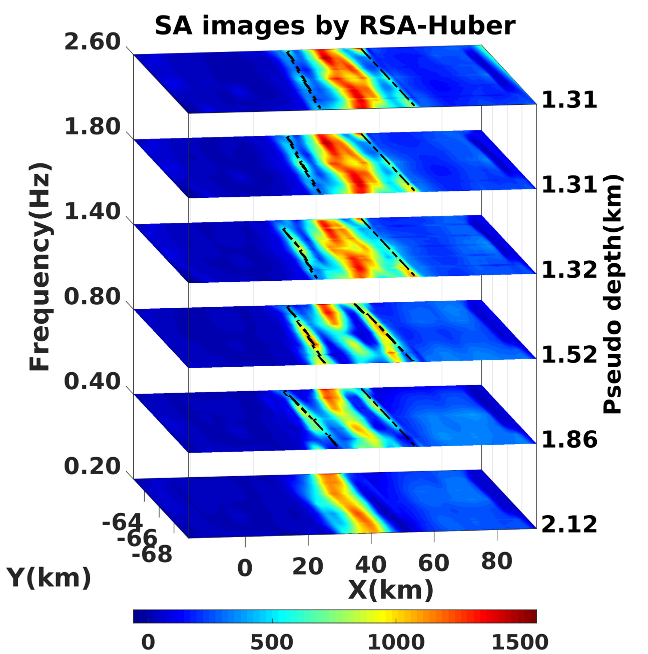

Fig. 20. SA images by the RSA method with the Huber norm. A boxcar DSA is used to enhance the response from the salt dome in the central part.

VI. Conclusion

We have developed an RSA method by applying a robust smoothing to the background field and robust interpolation of the fields from the real local receiver positions to virtual ones. Our model and case studies demonstrate that all the steps of the RSA method outlined above are generally required to ensure a robust solution. At the same time, the importance of one step over another depends on the specific situation, as explained below.

1) Background Field Smoothing: The importance of this step depends on the background field behavior. If the background field is selected in the area free from the influence of any geoelectrical anomaly and the noise level is low, there is no need in this step. Otherwise, it is recommended to smooth the background field by using step 1.

2) Robust Interpolation of EM Fields: The importance of this step also depends on the noise level and the presence of local inhomogeneities in the sea bottom. The latter is critical in the case of the MCSEM survey, where the EM fields in the sea-floor receivers can be strongly distorted by the local sea-bottom geoelectrical anomalies.

3) Robust Norms: The use of the robust norms is very important when the data are noisy. The application of the robust norms provides a higher spatial resolution as indicated in the second model study.

We have also developed and applied a robust inversion scheme to determine the RSA weights using the robust norms. By transforming frequencies into the pseudo depth based on the integrated sensitivity, the results produced by the RSA method could be assembled as a pseudo-3-D image of the subsurface geoelectrical structure. The synthetic model studies have demonstrated that the RSA method is stable to the noise in the data and also has a better spatial resolution with respect to the sea-bottom geoelectrical structures than the original SA technique. We have also applied the RSA method to the towed streamer EM data collected in the Barents Sea. This study shows that the RSA method enhances robustly the responses from the targets.

One of the major advantages of this method is that it can generate images of potential targets quickly for a large survey area compared to the rigorous inversion. It takes only a few minutes on PCs to run an SA imaging, while a full 3-D inversion would take several hours or even days on supercomputers. At the same time, this method could not be considered as a replacement of 3-D inversion because it provides just an image of the sea-bottom formations without reconstructing their electrical properties. This method is most suitable for a quick interpretation of the results of a regional reconnaissance survey and a real-time analysis of the acquired data and refining the survey lines in the target areas.

Thus, the developed method can be considered as an effective technique for real-time evaluation of offshore HC reservoir potential using the EM data.

Appendix

A. L_1-Norm

The L_1-norm of the residual can be reformulated as a weighted least-square norm

$$\|\mathbf{r}\|_{L_1} = (\mathbf{W}_{L_1}\mathbf{r}, \mathbf{W}_{L_1}\mathbf{r}) \tag{16}$$

with $W_{L_1} = \text{diag}(\frac{1}{|\mathbf{r}|^{\frac{1}{2}}})$. For L_1-norm, bigger weights are assigned to data corresponding to small residuals. However, datum with residual close to zero will be extremely overweighted and leads to a singularity problem.

B. Huber Norm

The kernel function for the Huber norm is defined as follows:

$$\rho_i(\mathbf{r}) = \begin{cases} r_i, & \text{if } |r_i| < a \\ \left(a|r_i| - \frac{1}{2}a^2\right)^{\frac{1}{2}}, & \text{if } |r_i| \geq a. \end{cases} \tag{17}$$

The diagonal weighting matrix can be calculated as follows:

$$W_{\rho i}(\mathbf{r}) = \begin{cases} 1, & \text{if } |r_i| < a \\ \dfrac{\left(a|r_i| - \frac{1}{2}a^2\right)^{\frac{1}{2}}}{[|r_i|^2 + e]^{\frac{1}{2}}}, & \text{if } |r_i| \geq a. \end{cases} \tag{18}$$

The Huber norm combines different treatments of small residuals and large ones. Only the part of data with residual bigger than a threshold is down-weighted. It is, therefore, more stable.

C. Hampel and Tukey Bisquare Norms

There are other robust norms, for example, the Hampel norm and the Tukey bisquare norm with the following kernels:

$$\rho_i^{Hampel}(\mathbf{r}) = \begin{cases} r_i, & \text{if } |r_i| < a \\ \left(a|r_i| - \frac{1}{2}a^2\right)^{\frac{1}{2}}, & \text{if } a \leq |r_i| < b \\ \left(a\dfrac{c|r_i| - \frac{1}{2}a^2}{c-b} - \dfrac{7}{6}a^2\right)^{\frac{1}{2}}, & \text{if } b \leq |r_i| < c \\ [a(b+c-a)]^{\frac{1}{2}}, & \text{otherwise} \end{cases} \tag{19}$$

$$\rho_i^{\text{bisquare}}(\mathbf{r}) = \begin{cases} \dfrac{1}{\sqrt{6}}a\left[1 - \left(1 - \left[\dfrac{|r_i|}{a}\right]^2\right)^3\right]^{\frac{1}{2}}, & \text{if } |r_i| < a \\ \dfrac{1}{\sqrt{6}}a, & \text{otherwise.} \end{cases} \tag{20}$$

The parameters in the robust norms, the coefficients a, b, c in (17)–(20), are determined based on some preassumed statistic distributions of the misfit residuals, which is usually a Gaussian distribution. For example, for the Huber norm, we can choose a equal to 1.44 of the median of the residuals, where the value 1.44 comes from the 85% confidence interval for the corresponding Gaussian distribution. There are many publications on robust estimation where the interested reader can find more details about the robust norms. For example, Huber's famous article "Huber, P. J., 1973, Robust regression: Asymptotics, conjectures, and Monte Carlo. Ann. Statist., 1, 799–821" is a perfect one.

Acknowledgment

The authors would like to thank PGS for providing the towed streamer EM data set in the Barents Sea.

References

[1] Á. H. Flosadóttir and S. Constable, "Marine controlled-source electromagnetic sounding: 1. Modeling and experimental design," *J. Geophys. Res.*, vol. 101, no. B3, pp. 5507–5517, Mar. 1996.
[2] S. Constable and C. S. Cox, "Marine controlled-source electromagnetic sounding: 2. The PEGASUS experiment," *J. Geophys. Res.*, vol. 101, no. B3, pp. 5519–5530, Mar. 1996.
[3] S. Constable and C. J. Weiss, "Mapping thin resistors and hydrocarbons with marine EM methods: Insights from 1D modeling," *Geophysics*, vol. 71, no. 2, pp. G43–G51, Mar. 2006.
[4] C. J. Weiss and S. Constable, "Mapping thin resistors and hydrocarbons with marine EM methods, Part II—Modeling and analysis in 3D," *Geophysics*, vol. 71, no. 6, pp. G321–G332, 2006.
[5] S. Constable and L. J. Srnka, "An introduction to marine controlled-source electromagnetic methods for hydrocarbon exploration," *Geophysics*, vol. 72, no. 2, pp. WA3–WA12, Mar. 2007.
[6] M. Lien and T. Mannseth, "Sensitivity study of marine CSEM data for reservoir production monitoring," *Geophysics*, vol. 73, no. 4, pp. F151–F163, Jul. 2008.
[7] A. Orange, K. Key, and S. Constable, "The feasibility of reservoir monitoring using time-lapse marine CSEM," *Geophysics*, vol. 74, no. 2, pp. F21–F29, Mar. 2009.
[8] N. Black and M. S. Zhdanov, "Monitoring of hydrocarbon reservoirs using marine CSEM method," in *Proc. SEG Annu. Meeting*, Jan. 2009.
[9] S. Constable, "Ten years of marine CSEM for hydrocarbon exploration," *Geophysics*, vol. 75, no. 5, pp. 75A67–75A81, Sep. 2010.
[10] K. Key, "Marine electromagnetic studies of seafloor resources and tectonics," *Surv. Geophys.*, vol. 33, no. 1, pp. 135–167, Jan. 2012.
[11] S. Constable, P. K. Kannberg, and K. Weitemeyer, "Vulcan: A deep-towed CSEM receiver," *Geochem. Geophys. Geosyst.*, vol. 17, no. 3, pp. 1042–1064, Mar. 2016.
[12] A. McKay, J. Mattson, and Z. Du, "Towed streamer EM–reliable recovery of sub-surface resistivity," *First Break*, vol. 33, no. 4, pp. 75–85, Apr. 2015.
[13] Z. Du, G. Namo, V. Charoing, and C. Reiser, "Improved reservoir characterization from integration of towed streamer em and dual-sensor broadband seismic data," in *Proc. 79th EAGE Conf. Exhib.*, Paris, France, Jun. 2017.
[14] D. Sherman, P. Kannberg, and S. Constable, "Surface towed electromagnetic system for mapping of subsea Arctic permafrost," *Earth Planet. Sci. Lett.*, vol. 460, pp. 97–104, Feb. 2017.
[15] A. Gribenko and M. Zhdanov, "Rigorous 3D inversion of marine CSEM data based on the integral equation method," *Geophysics*, vol. 72, no. 2, pp. WA73–WA84, Mar. 2007.
[16] M. S. Zhdanov, L. Wan, A. Gribenko, M. Cuma, K. Key, and S. Constable, "Rigorous 3D inversion of marine magnetotelluric data in the area with complex bathymetry," in *Proc. SEG Annu. Meeting*, 2009.
[17] M. S. Zhdanov, M. Endo, D. Yoon, M. Čuma, J. Mattsson, and J. Midgley, "Anisotropic 3D inversion of towed-streamer electromagnetic data: Case study from the Troll West Oil Province," *Interpretation*, vol. 2, no. 3, pp. SH97–SH113, Aug. 2014.
[18] D. Yoon, M. S. Zhdanov, J. Mattsson, H. Cai, and A. Gribenko, "A hybrid finite-difference and integral-equation method for modeling and inversion of marine controlled-source electromagnetic data," *Geophysics*, vol. 81, no. 5, pp. E323–E336, Sep. 2016.
[19] K. Key, "MARE2DEM: A 2-D inversion code for controlled-source electromagnetic and magnetotelluric data," *Geophys. J. Int.*, vol. 207, no. 1, pp. 571–588, Oct. 2016.
[20] F. Wang, J. P. Morten, and K. Spitzer, "Anisotropic three-dimensional inversion of CSEM data using finite-element techniques on unstructured grids," *Geophys. J. Int.*, vol. 213, no. 2, pp. 1056–1072, 2018.
[21] M. S. Zhdanov, D. Yoon, and J. Mattsson, "Rapid imaging of towed streamer EM data using the optimal synthetic aperture method," *IEEE Geosci. Remote Sens. Lett.*, vol. 14, no. 2, pp. 262–266, Feb. 2017.
[22] Y. Fan, R. Snieder, E. Slob, J. Hunziker, and J. Singer, "Steering and focusing diffusive fields using synthetic aperture," *(Europhys. Lett.)*, vol. 95, no. 3, 2011, Art. no. 34006.
[23] Y. Fan *et al.*, "Synthetic aperture controlled source electromagnetics," *Geophys. Res. Lett.*, vol. 37, no. 13, Jul. 2010.
[24] Y. Fan *et al.*, "Increasing the sensitivity of controlled-source electromagnetics with synthetic aperture," *Geophysics*, vol. 77, no. 2, pp. E135–E145, Mar. 2012.
[25] D. Yoon and M. S. Zhdanov, "Optimal synthetic aperture method for marine controlled-source EM surveys," *IEEE Geosci. Remote Sens. Lett.*, vol. 12, no. 2, pp. 414–418, Feb. 2015.

[26] X. Tu and M. S. Zhdanov, "Robust optimal synthetic aperture imaging of towed streamer electromagnetic data," in *Proc. SEG Tech. Program Expanded Abstr.*, Aug. 2018, pp. 903–908.

[27] A. T. Djanni, A. Ziolkowski, and D. Wright, "Electromagnetic induction noise in a towed electromagnetic streamer," *Geophysics*, vol. 81, no. 3, pp. E187–E199, May 2016.

[28] D. Connell and K. Key, "A numerical comparison of time and frequency-domain marine electromagnetic methods for hydrocarbon exploration in shallow water," *Geophys. Prospecting*, vol. 61, no. 1, pp. 187–199, Jan. 2013.

[29] X. Tu, "Time domain approach for multi-channel transient electromagnetic modeling," M.S. thesis, Inst. Geol. Geophys., Chin. Acad. Sci., Beijing, China, 2015.

[30] M. S. Zhdanov, *Inverse Theory and Applications in Geophysics*, 2nd ed. Oxford, U.K.: Elsevier, 2015.

[31] D. Garcia, "Robust smoothing of gridded data in one and higher dimensions with missing values," *Comput. Statist. Data Anal.*, vol. 54, no. 4, pp. 1167–1178, Apr. 2010.

[32] A. Tarantola, *Inverse Problem Theory and Methods for Model Parameter Estimation*. Philadelphia, PA, USA: Society for Industrial and Applied Mathematics, 2005.

[33] J. F. Claerbout and F. Muir, "Robust modeling with erratic data," *Geophysics*, vol. 38, no. 5, pp. 826–844, Oct. 1973.

[34] A. Guitton and W. W. Symes, "Robust inversion of seismic data using the Huber norm," *Geophysics*, vol. 68, no. 4, pp. 1310–1319, Jul. 2003.

[35] A. D. Chave, D. J. Thomson, and M. E. Ander, "On the robust estimation of power spectra, coherences, and transfer functions," *J. Geophys. Res.*, vol. 92, no. B1, p. 633, Feb. 2008.

[36] G. D. Egbert and J. R. Booker, "Robust estimation of geomagnetic transfer functions," *Geophys. J. Int.*, vol. 87, no. 1, pp. 173–194, Oct. 1986.

[37] A. G. Jones, A. D. Chave, G. Egbert, D. Auld, and K. Bahr, "A comparison of techniques for magnetotelluric response function estimation," *J. Geophys. Res.*, vol. 94, no. B10, pp. 14201–14213, Oct. 1989.

[38] D. Sutarno and K. Vozoff, "Robust M-Estimation of Magnetotelluric Impedance Tensors," *Explor. Geophys.*, vol. 20, no. 3, pp. 383–398, Jun. 1989.

[39] P. J. Huber, "Robust regression: Asymptotics, conjectures and Monte Carlo," *Ann. Statist.*, vol. 1, no. 5, pp. 799–821, 1973.

Xiaolei Tu received the B.S. degree in geophysics from the Ocean University of China, Qingdao, China, in 2012, and the M.Sc. degree in geophysics from the Institute of Geology and Geophysics, Chinese Academy of Sciences, Beijing, China, in 2015. He is currently pursuing the Ph.D. degree with The University of Utah, Salt Lake City, UT, USA.

His research interests include the computational and mathematical methods of electromagnetic geophysics and the joint inversion of multiphysics geophysical data.

Michael S. Zhdanov received the M.Sc. degree in geophysics from the Moscow Gubkin State University of Oil and Gas, Moscow, Russia, in 1968, and the Ph.D. degree in physics and mathematics from the Moscow State University, Moscow, in 1970.

He was the Founding Director of the Geoelectromagnetic Research Institute, Russian Academy of Sciences, Moscow, and also the Deputy Director of the Institute of Terrestrial Magnetism, Ionosphere and Radio Wave Propagation, Russian Academy of Sciences. He is currently a Distinguished Professor of the Department of Geology and Geophysics, The University of Utah, Salt Lake City, UT, USA, the Director of the Consortium for Electromagnetic Modeling and Inversion (CEMI), and the CEO and Chairman of TechnoImaging, Salt Lake City, UT, USA. He is also an Honorary Gauss Professor of the Göttingen Academy of Sciences, Göttingen, Germany, a fellow of the Russian Academy of Natural Sciences, a fellow of the Electromagnetics Academy USA, a Honorary Professor of the China National Centre for Geological Exploration Technology, Beijing, China, and a Honorary Member of the Society of Exploration Geophysicists. His research interests include fundamental and applied geophysics, inversion theory, electromagnetic theory and methods, as well as integration and joint inversion of multiphysics data.